Angular distribution of γ rays from neutron-induced compound states of ^{140}La

T. Okudaira,[1] S. Takada,[2] K. Hirota,[1] A. Kimura,[3] M. Kitaguchi,[1] J. Koga,[2] K. Nagamoto,[1,*] T. Nakao,[3,†] A. Okada,[1,‡] K. Sakai,[3] H. M. Shimizu,[1] T. Yamamoto,[1] and T. Yoshioka[2]

[1]*Nagoya University, Furocho, Chikusa, Nagoya 464-8602, Japan*

[2]*Kyushu University, 744 Motooka, Nishi, Fukuoka 819-0395, Japan*

[3]*Japan Atomic Energy Agency, 2-1 Shirane, Tokai 319-1195, Japan*

(Received 9 October 2017; published 27 March 2018)

The angular distribution of individual γ rays, emitted from a neutron-induced compound-nuclear state via radiative capture reaction of ^{139}La(n,γ) has been studied as a function of incident neutron energy in the epithermal region by using germanium detectors. An asymmetry A_{LH} was defined as $(N_{\mathrm{L}} - N_{\mathrm{H}})/(N_{\mathrm{L}} + N_{\mathrm{H}})$, where N_{L} and N_{H} are integrals of low- and high-energy region of a neutron resonance respectively, and we found that A_{LH} has the angular dependence of $(A\cos\theta_\gamma + B)$, where θ_γ is the emitted angle of γ rays, with $A = -0.3881 \pm 0.0236$ and $B = -0.0747 \pm 0.0105$ in 0.74 eV p-wave resonance. This angular distribution was analyzed within the framework of interference between s- and p-wave amplitudes in the entrance channel to the compound-nuclear state, and it is interpreted as the value of the partial p-wave neutron width corresponding to the total angular momentum of the incident neutron combined with the weak matrix element, in the context of the mechanism of enhanced parity-violating effects. Additionally, we use the result to quantify the possible enhancement of the breaking of time-reversal invariance in the vicinity of the p-wave resonance.

DOI: 10.1103/PhysRevC.97.034622

I. INTRODUCTION

The magnitude of parity-violating effects in effective nucleon-nucleon interactions is 10^{-7}, as observed in the helicity dependence of the total cross section between nucleons [1–3]. Extremely large parity violation (P violation) was found in the helicity dependence of the neutron absorption cross section in the vicinity of the p-wave resonance of $^{139}\mathrm{La} + n$ [4]. The helicity dependence was measured as the ratio of the helicity-dependent cross section to the p-wave-resonance cross section, referred to as longitudinal asymmetry, which amounts to $(9.56 \pm 0.35)\%$. The large P violation was explained as the interference between the amplitudes of the p-wave resonance and the neighboring s-wave resonance [5,6]. Longitudinal asymmetry was intensively studied in neutron transmission and in (n,γ) measurements [7–10]. The γ-ray energy dependence of the asymmetry was not found, which implies that interference occurs in the entrance channel to the compound state and not in the exit channel [11]. Under this assumption, the longitudinal asymmetry A_{L} is given by

$$A_{\mathrm{L}} \simeq -\frac{2xW}{E_p - E_s}\sqrt{\frac{\Gamma_s^n}{\Gamma_p^n}}, \tag{1}$$

assuming s-wave and p-wave resonances, where E_s and E_p are their respective energies, Γ_s^n and Γ_p^n are the corresponding neutron widths, and W is the weak matrix element. The value of x is defined as $x^2 = \Gamma^n_{p,j=\frac{1}{2}}/\Gamma_p^n$, where $\Gamma^n_{p,j=\frac{1}{2}}$ is the partial neutron width for the total angular momentum of the incident neutron $j = 1/2$. The detailed definition of x is described in Appendix E. A theoretical model explaining the large enhancement of P violation in compound states was studied and summarized in Ref. [12]. The enhancement mechanism is expected to be applicable to P- and time-violating (T-violating) interactions and to enable highly sensitive explorations of charge-parity-violating (CP-violating) interactions beyond the standard model of elementary particles. The sensitivity of T violation can be quantified in relation to the magnitude of P violation as a function of x [13,14].

However, the values of x and W have not yet been measured individually. The value of x can be extracted from the energy dependence of the angular distribution of γ rays from a p-wave resonance in a neutron-induced compound nucleus, which has not yet been measured. Theoretically, it can be deduced by assuming interference between partial waves in the entrance channel [15].

In this paper we report measurement results of the angular distribution of individual γ rays emitted from the 0.74 eV p-wave resonance of $^{139}\mathrm{La} + n$ as a function of incident neutron energy.

II. EXPERIMENT

A. Experimental setup

The angular distribution of individual γ rays through the radiative capture reactions induced by epithermal neutrons

*Present Address: Denso Corporation, 1-1, Showa-cho, Kariya, Aichi 448-8661, Japan.

†Present Address: Nagoya University, Furocho, Chikusa, Nagoya 464-8602, Japan.

‡Present Address: New Japan Radio Corporation, 3-10, Nihonbashi Yokoyama-cho,Chuo-ku, Tokyo 103-8456, Japan.

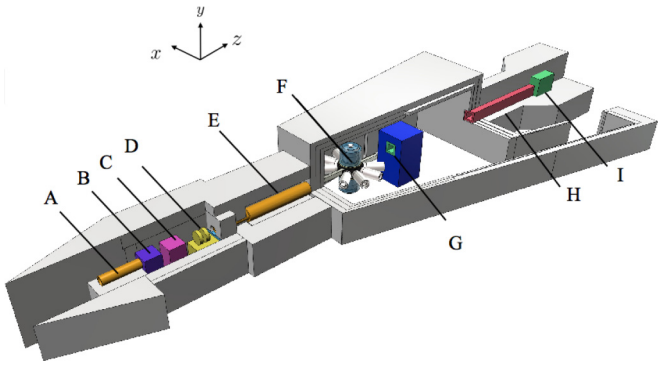

FIG. 1. Schematic of the ANNRI installed at beamline 04 of MLF at J-PARC: (A) collimator, (B) T0-chopper, (C) neutron filter, (D) disk chopper, (E) collimator, (F) germanium detector assembly, (G) collimator, (H) boron resin, and (I) beam stopper (iron).

was measured by introducing a pulsed neutron beam into the Accurate Neutron–Nucleus Reaction Measurement Instrument (ANNRI) installed at beamline BL04 of the Material and Life Science Experimental Facility (MLF) of the Japan Proton Accelerator Research Complex (J-PARC), as shown in Fig. 1 [16]. The primary proton-beam pulses were injected to the neutron-production target in a single-bunch mode at a repetition rate of 25 Hz and an average beam power of 150 kW during the measurement. The disk chopper was operated synchronously with the proton injection for the suppression of low-energy neutrons, to avoid frame overlap. The beam collimation was adjusted to define the neutron beam in a 22-mm-diameter circle on the target, placed 21.5 m from the moderator surface [17]. A lead plate (thickness 37.5 mm) was placed in the upstream optics to suppress the γ-ray background. The z axis is defined in the beam direction, the y axis is the vertical upward axis, and the x axis is perpendicular to them, thus xyz forms a right-handed frame.

An assembled set of high-purity germanium spectrometers were used to detect γ rays emitted from the target [18]. The configuration of the germanium spectrometer assembly is shown in Fig. 2.

The assembly consisted of two types of detector units: type A (Fig. 3) and type B (Fig. 4).

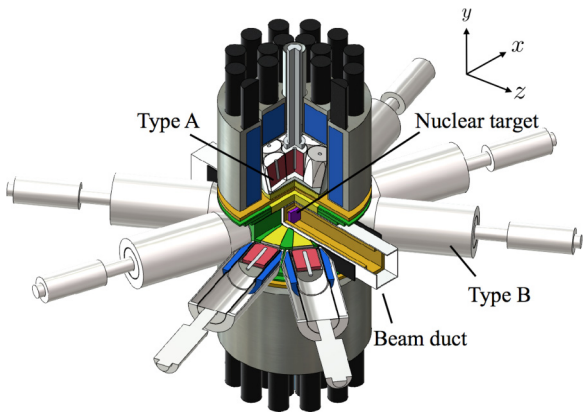

FIG. 2. Configuration of germanium spectrometer assembly.

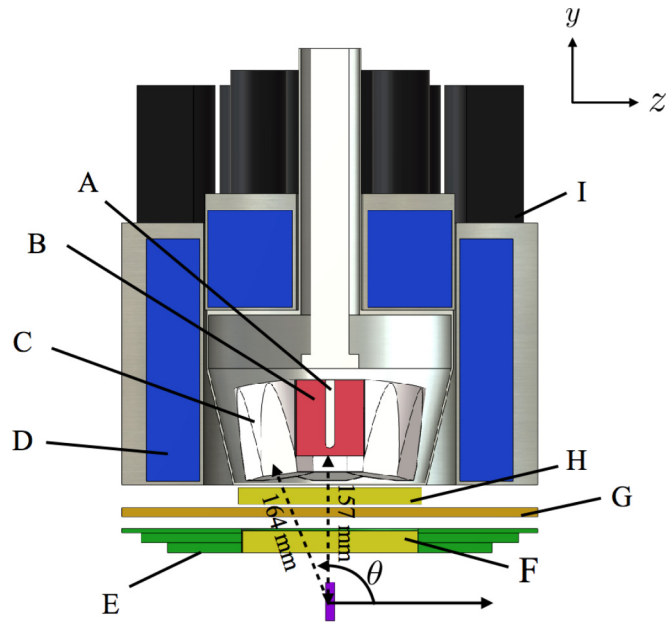

FIG. 3. Schematics of the upper seven type-A detectors: (A) electrode, (B) germanium crystal, (C) aluminum case, (D) BGO crystal, (E) γ-ray shield (Pb collimator), (F) neutron shield 1 (LiH 22.3 mm thick), (G) neutron shield 2 (LiF 5 mm thick), (H) neutron shield 3 (LiH 17.3 mm thick), and (I) photomultiplier tube for BGO crystal.

Two combined seven type-A detectors were placed above and below the target. The shape of the type-A detector was hexagonal to enable clustering, as shown in Fig. 3. The polar angles between the center of the target and the center of the crystal surface facing the target were $\theta = 71^\circ$, 90°, and 109°.

Eight type-B detectors were placed on the xz plane at $\theta = 36^\circ, 72^\circ, 108^\circ$, and 144°, as shown in Fig. 4. The central crystals of the upper and lower type-A detectors are denoted d1 and d8, respectively, and the other six surrounding detectors are denoted d2–d7 (d9–d14). The names of each type-B detectors are shown in Fig. 4. In our measurement, d16 and d17 were not used.

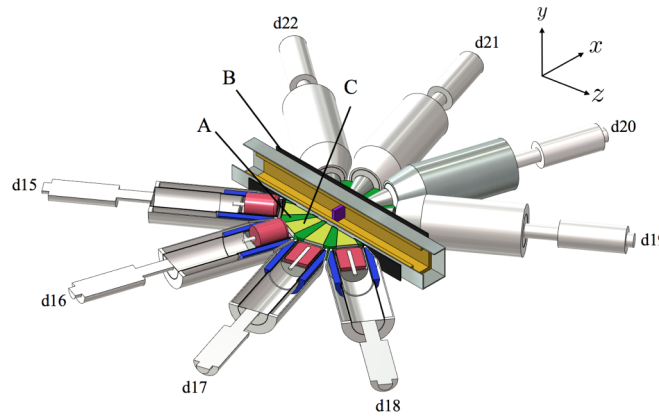

FIG. 4. Schematics of type-B detectors: (A) Pb collimator, (B) carbon board, and (C) LiH powder.

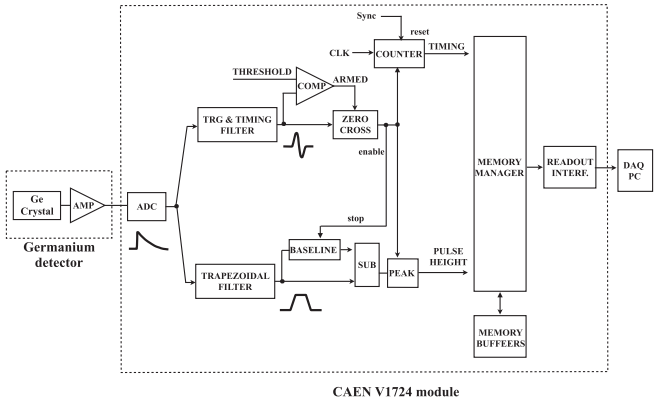

FIG. 5. Block diagram of signal processing. A signal from the germanium detector is divided into two branches: one for the timing and triggering and the other for the pulse height. In the branch of timing and triggering, the signal is converted to a bipolar signal. Signals over a threshold are triggered and the time of zero crossing determines the timing of the signal. In the branch of the pulse height, the signal is converted to a trapezoidal signal and the height of the trapezoidal from a baseline determines the pulse height of the signal.

All germanium crystals were operated at a temperature of 77 K. The typical energy resolution for the 1.332 MeV γ rays was 4.2 keV.

The output signal from each crystal was processed independently. The block diagram of the signal processing is shown in Fig. 5. The output signals from the preamplifier were fed into the signal-processing module CAEN V1724 [19], which stored the combination of the pulse height digitized by using the peak-sensitive ADC and the timing of the zero-cross point measured from the timing pulse of the injection of the primary proton beam bunch t^{m}. The CAEN V1724 module transferred the stored data to the computer when 1024 event data are accumulated in the local buffer. Two pulses temporarily closer than 0.4 μs were processed as a single event, while their pulse heights were recorded as a zero when their time difference was in the range of 0.4 to 3.2 μs.

Their response functions were simulated by using GEANT4.9.6. Definitions of the symbols to describe the detector characteristics and results of the simulation are discussed in detail in Appendix A.

The relation between the pulse height of photopeaks and the deposited γ-ray energy was determined by observing γ rays emitted from neutron-capture reactions by aluminum. The effective photopeak efficiency, including the solid angle coverage of each detector unit, was determined relatively based on the assumption that prompt γ rays from $^{14}\mathrm{N}(n,\gamma)$ of a melamine target were emitted isotropically. The relative photopeak efficiencies are shown in Table III.

B. Measurement

The target was a natural-abundance lanthanum plate at room temperature, with the dimensions of 40 mm × 40 mm × 1 mm, and with a purity of 99.9%. The total number of γ-ray events detected in the experiment is denoted I_γ. Here, the

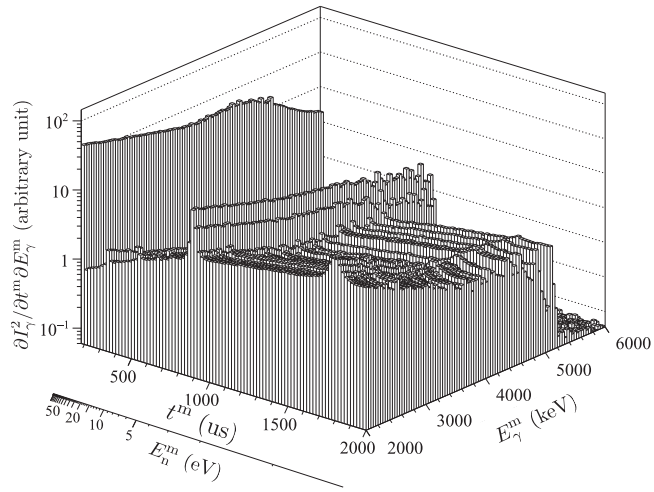

FIG. 6. $\partial^2 I_\gamma/\partial t^{\mathrm{m}}\partial E_\gamma^{\mathrm{m}}$ two-dimensional histogram of γ rays with the lanthanum target as a function of timing t^{m} and deposited γ-ray energy E_γ^{m}. The corresponding neutron energy E_n^{m} is also shown.

corresponding neutron energy E_n^{m} is defined as

$$E_n^{\mathrm{m}} = \frac{m_n}{2}\left(\frac{L}{t^{\mathrm{m}}}\right)^2, \tag{2}$$

where m_n is the neutron mass and L is the distance between the target and the moderator surface. The deposited γ-ray energy E_γ^{m} obtained from the calibration of the pulse height is defined as well. The results obtained are shown as a two-dimensional histogram corresponding to $\partial^2 I_\gamma/\partial t^{\mathrm{m}}\partial E_\gamma^{\mathrm{m}}$ in Fig. 6. The histograms projected on t^{m} and E_γ^{m} are shown in Figs. 7 and 8, respectively. In Fig. 7, γ-ray events with E_γ^{m} are integrated and relatively corrected by the incident beam spectrum for t^{m}. The incident beam spectrum was obtained by measuring the 477.6 keV γ rays in $^{10}\mathrm{B}(n,\alpha\gamma)^7\mathrm{Li}$ reactions, with a boron target placed at the detector center. The small peak at $t^{\mathrm{m}} \sim 1800$ μs is a p-wave resonance, and the $1/v$ component is the tail of an s-wave resonance in the negative-energy region as listed in Table I.

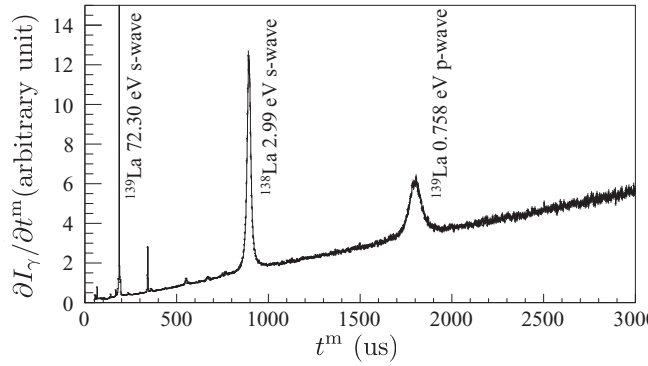

FIG. 7. γ-ray counts relatively corrected by the incident beam intensity as a function of t^{m} for $E_\gamma^{\mathrm{m}} \geqslant 2$ MeV, which is referred as $\partial I_\gamma/\partial t^{\mathrm{m}}$.

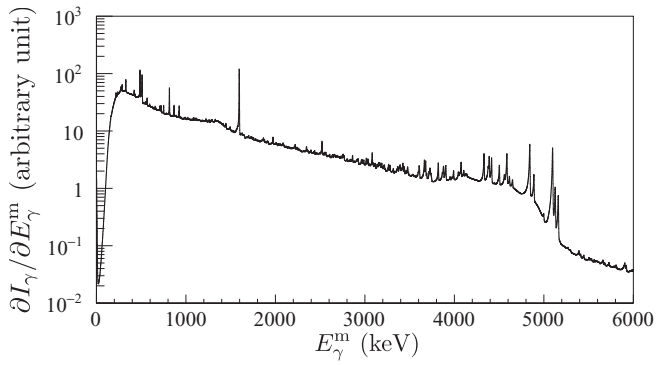

FIG. 8. Pulse-height spectrum of γ rays $\partial I_\gamma/\partial E_\gamma^{\rm m}$ from the (n,γ) reaction with a lanthanum target as a function of $E_\gamma^{\rm m}$.

The neutron energy in the center-of-mass system E_n is given as

$$E_n = \frac{m_n m_A}{m_n + m_A}\left(\frac{\boldsymbol{p}_n}{m_n} - \frac{\boldsymbol{p}_A}{m_A}\right)^2, \tag{3}$$

where $\boldsymbol{p}_n$ is the momentum of the neutron in the laboratory system, $\boldsymbol{p}_A$ is nuclear momentum of the target, and m_A is the mass of the nucleus of the target.

The beam divergence is sufficiently small and the following can be assumed:

$$\boldsymbol{p}_n = \sqrt{2m_n E_n}\,\boldsymbol{e}_z, \tag{4}$$

where $\boldsymbol{e}_z$ is the unit vector parallel to the beam axis. The resonance energy E_r and the total width Γ_r of the rth resonance, which are obtained by fitting $\partial I_\gamma/\partial t^{\rm m}$ with Eq. (D1) are shown in Table I, together with the published values. The formalism of the neutron-absorption cross section is described in Appendix B. The pulse shape of the neutron beam and the Doppler effect of the target nucleus are considered, as shown in Appendixes C and D, respectively. Because the neutron width of the p-wave resonance is negligibly smaller than γ-ray width of the p-wave resonance, the total width of the p-wave resonance was used as the γ-ray width of the p-wave resonance. The fit result is shown in Fig. 9.

The level scheme related to the ^{139}La$(n,\gamma)^{140}$La reaction is schematically shown in Fig. 10 [24]. The γ-ray transitions to the ground state and low excited states of ^{140}La were observed as shown in the expanded $\partial I_\gamma/\partial E_\gamma^{\rm m}$ (Fig. 11). The highest peak at $E_\gamma^{\rm m} = 5161$ keV corresponds to the γ-ray direct transition to the ground state of ^{140}La (spin of the final state: $F = 3$), the middle peak corresponds to the overlap of two transitions at $E_\gamma^{\rm m} = 5131$ keV and 5126 keV to the first- and second-excited states at excited energy 30 keV (F= 5), 35 keV ($F = 2$), and the lower peak at $E_\gamma^{\rm m} = 5098$ keV corresponds to the excited state at 63 keV ($F = 4$).

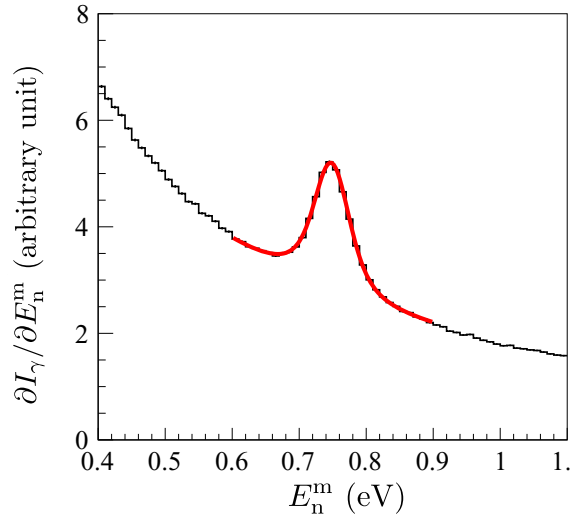

FIG. 9. Fit result of p-wave resonance. The curve shows the best fit.

Figure 12 shows the magnified two-dimensional histogram of $\partial^2 I_\gamma/\partial t^{\rm m}\partial E_\gamma^{\rm m}$ in the vicinity of the p-wave resonance and the γ-ray transition to the ground state of ^{140}La. The p-wave resonance was selectively observed only for two ridges corresponding to the transition at $E_\gamma^{\rm m} = 5161$ keV and the sum of transitions at $E_\gamma^{\rm m} = 5131$ keV, 5126 keV, but not for the ridge at $E_\gamma^{\rm m} = 5098$ keV. According to the dependence of $\partial^2 I_\gamma/\partial t^{\rm m}\partial E_\gamma^{\rm m}$ on $t^{\rm m}$, and therefore on the incident neutron energy, the s-wave resonance in the negative region contributes to all three γ-ray transitions, and the p-wave resonance contributes to the 5161 keV transition and 5131 keV and/or 5126 keV transitions.

C. Angular distribution

Hereafter, we concentrate on the 5161 keV transition to the ground state of ^{140}La in order to study the interference between the s- and p-wave amplitudes.

The photopeak efficiency, including both the detection efficiency and the solid-angle coverage, was readjusted by using

TABLE I. Resonance parameters of ^{139}La. $\Gamma_r^{nl_r}$ is a reduced neutron width.

r	Published values						This work	
	E_r [eV]	J_r	l_r	Γ_r^γ [meV]	$g_r\Gamma_r^n$ [meV]	$g_r\Gamma_r^{nl_r}$ [meV]	E_r [eV]	Γ_r^γ [meV]
1	-48.63[a]	4[a]	0	62.2[a]		82[a]		
2	0.758 ± 0.001[b]		1	40.11 ± 1.94[c]	$(5.6 \pm 0.5) \times 10^{-5}$[c]		0.740 ± 0.002	40.41 ± 0.76
3	72.30 ± 0.05[b]		0	75.64 ± 2.21[c]	11.76 ± 0.53[c]			

[a]Taken from Refs. [20,21].
[b]Taken from Ref. [22].
[c]Calculated from Refs. [22,23].

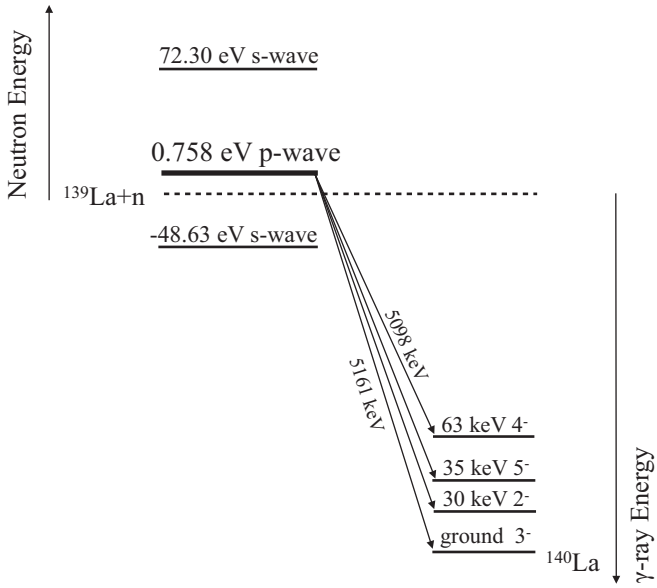

FIG. 10. Transitions from $^{139}\mathrm{La}+n$ to $^{140}\mathrm{La}$. Dashed line shows separation energy of $^{139}\mathrm{La}+n$.

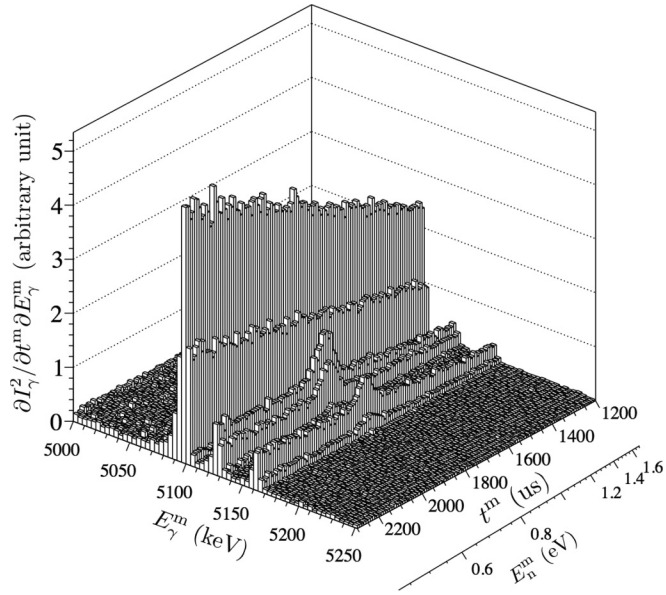

FIG. 12. Magnified two-dimensional histogram.

the photopeak counts of the γ rays at $E_\gamma^{\mathrm{m}} = 5262$ keV from the $^{14}\mathrm{N}(n,\gamma)$ reaction measured using the melamine target. It can be reasonably assumed that the γ rays are emitted isotropically, because $^{14}\mathrm{N}$ does not have any resonance below 400 eV and p-wave or higher angular-momentum components of the incident neutron are negligibly small in this energy region.

The photopeak counts of the 5161 keV transition were determined by subtracting the background counts caused by Compton scattering of the more energetic γ rays from targets other than the lanthanum target. To evaluate the background, two energy regions were used: (I) 5200 keV $\leqslant E_\gamma^{\mathrm{m}} \leqslant$ 5290 keV and (II) 4900 keV $\leqslant E_\gamma^{\mathrm{m}} \leqslant$ 4980 keV. The contribution of Compton scattering of γ rays corresponding to the three photopeaks are contained in region (II). The amount of this contribution from Compton scattering is estimated by using the response function $\bar{\psi}$ given in Eq. (A2) and obtained by simulation. The background in region (II) is estimated by

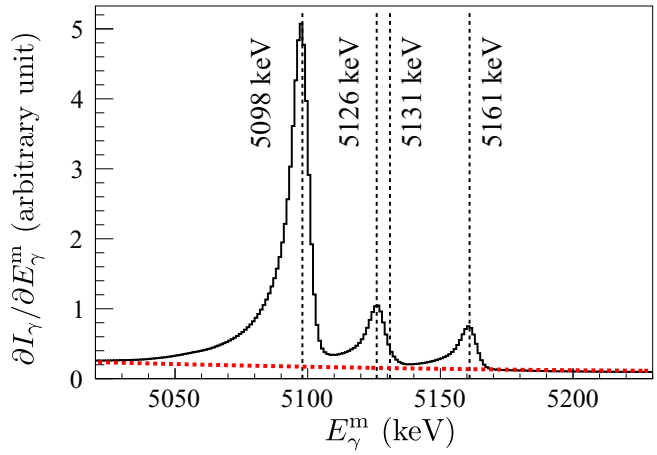

FIG. 11. Expanded $\partial I_\gamma/\partial E_\gamma^{\mathrm{m}}$. The dotted line shows the background determined by the simulation.

subtracting the Compton contribution from the γ-ray counts in region (II). The background is estimated by using a best-fit third-order polynomial of E_γ^{m} in regions (I) and (II).

There still remains a possible contamination of prompt γ rays from impurities overlapping with the 5161 keV photopeak. The possible contamination was examined over the entire pulse-height spectrum and was determined to be less than 0.08% of the photopeak. The possibility of contamination was neglected because the determined upper limit of 0.08% is smaller than the statistical error of the photopeak.

According to the data-acquisition system, two pulses detected within 3.2 μs did not have amplitude information, which amounted to 2% of the total γ-ray counts in the vicinity of the p-wave resonance. The 2% loss was corrected in the following analysis.

Two pulses detected within 0.4 μs were processed as a single pulse. The corresponding loss of the events were estimated as 0.2% of the total γ-ray counts in the vicinity of the p-wave resonance, which is negligibly small compared with the statistical error of the corresponding γ-ray counts and is ignored in the following analysis.

Equation (D1) was extended to describe the angular distribution of γ rays as

$$\frac{\partial^2 I_\gamma}{\partial t^{\mathrm{m}}\partial\Omega_\gamma}(t^{\mathrm{m}},\Omega_\gamma)d = I_0 \int dE' d^3 p_A \Phi(t^{\mathrm{m}},E',\boldsymbol{p}_A) \times \frac{d\sigma_{n\gamma}}{d\Omega_\gamma}(E,\Omega_\gamma), \tag{5}$$

$$\Phi(t^{\mathrm{m}},E',\boldsymbol{p}_A) = \frac{\partial^2\phi}{\partial E_n \partial t}\left(E', t^{\mathrm{m}} - L\sqrt{\frac{m_n}{2E'}}\right) \times \frac{1}{(2\pi m_A k_{\mathrm{B}} T)^{3/2}} e^{-p_A^2/2m_A k_{\mathrm{B}} T} \times \frac{1}{\sigma_{\mathrm{t}}(E)}(1 - e^{-n\sigma_{\mathrm{t}}(E)\Delta z}). \tag{6}$$

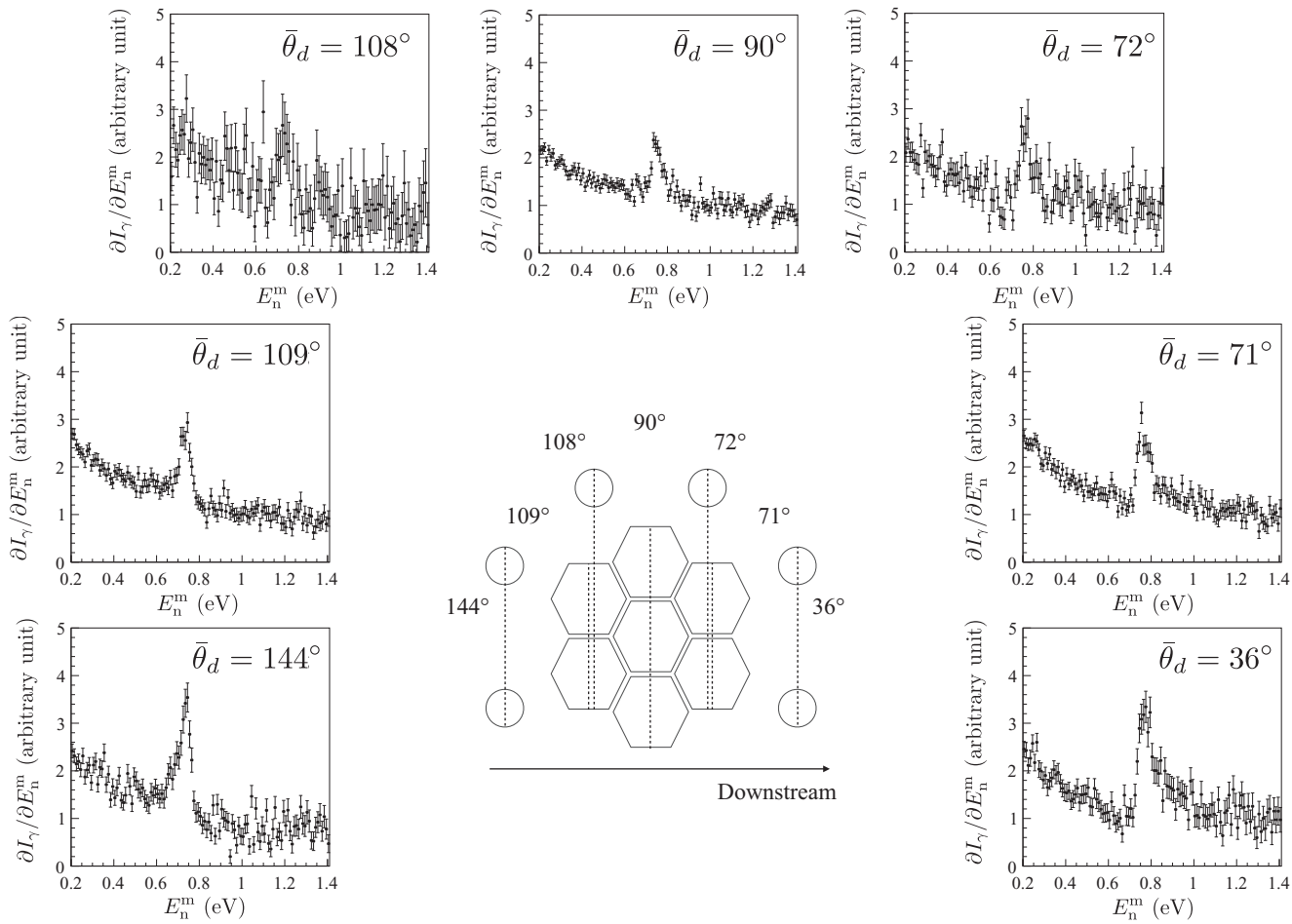

FIG. 13. $\partial N/\partial t^m$ in the vicinity of the p-wave resonance for each $\bar{\theta}_d$. The central figure shows degrees in the direction of neutron momentum of the type-A detectors and the type-B detectors. The hexagons and the circles in the center of the figure denote each crystal of the type-A detector and type-B detector, respectively.

The γ-ray counts to be measured by the dth detector can be written as

$$\frac{\partial N}{\partial t^m}(t^m,\bar{\theta}_d) = \int_{\Omega_d} d\Omega_\gamma \int_{(E_\gamma^m)_d^{w-}}^{(E_\gamma^m)_d^{w+}} d\left(E_\gamma^m\right)_d \times \frac{\partial^2 I_\gamma}{\partial t^m \partial \Omega_\gamma}(t^m,\Omega_\gamma)\psi_d\left(E_\gamma,\Omega_\gamma,\left(E_\gamma^m\right)_d\right), \quad (7)$$

where the photopeak region is taken as the full width at quarter maximum, which implies $w = 1/4$. Figure 13 shows $N(t^m,\bar{\theta}_d)$ for 5161 keV γ rays. The peak shape of the p-wave resonance varies according to $\bar{\theta}_d$. Here, we define N_L and N_H as

$$N_L(\theta_\gamma) = \int_{E_p-2\Gamma_p}^{E_p} \frac{\partial N}{\partial t^m}(t',\bar{\theta}_\gamma)dt^m \frac{dt^m}{dE_n}dE_n,$$
$$N_H(\theta_\gamma) = \int_{E_p}^{E_p+2\Gamma_p} \frac{\partial N}{\partial t^m}(t',\bar{\theta}_\gamma)dt^m \frac{dt^m}{dE_n}dE_n. \quad (8)$$

The definitions of N_L and N_H are shown in Fig. 14. The angular dependencies of N_L and N_H are shown in Fig. 15. Because N_L and N_H have certain angular dependence in Fig. 15, we define an asymmetry between N_L and N_H to determine the angular dependence of the shape of p-wave resonance as

$$A_{LH} = \frac{N_L - N_H}{N_L + N_H}. \quad (9)$$

The angular dependence of A_{LH} is shown in Fig. 16. The asymmetry A_{LH} has a correlation with $\cos\bar{\theta}_\gamma$ as

$$A_{LH} = (A\cos\bar{\theta}_\gamma + B), \quad (10)$$

where

$$A = -0.3881 \pm 0.0236, \quad B = -0.0747 \pm 0.0105, \quad (11)$$

which are the best-fit results of Fig. 16. This result implies that clear energy dependence of the angular distribution of γ rays was observed.

The x value of the p-wave resonance can be obtained by using this result. The analysis and the interpretation of this result are discussed in Secs. III and IV.

III. ANALYSIS

Our experimental results are analyzed by using the formulation of possible angular correlations of individual γ rays

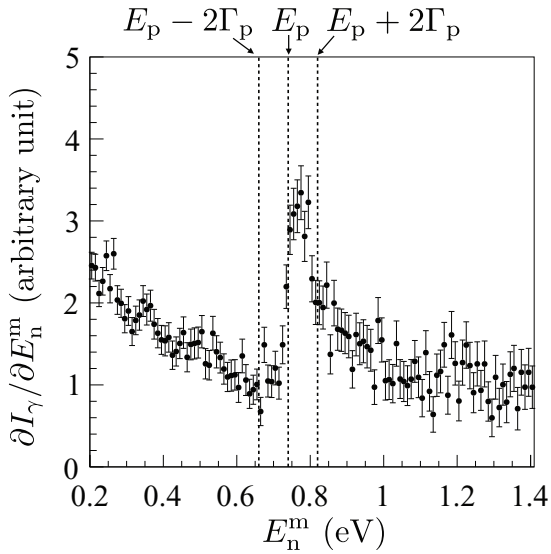

FIG. 14. Visualization of the definitions of N_L and N_H.

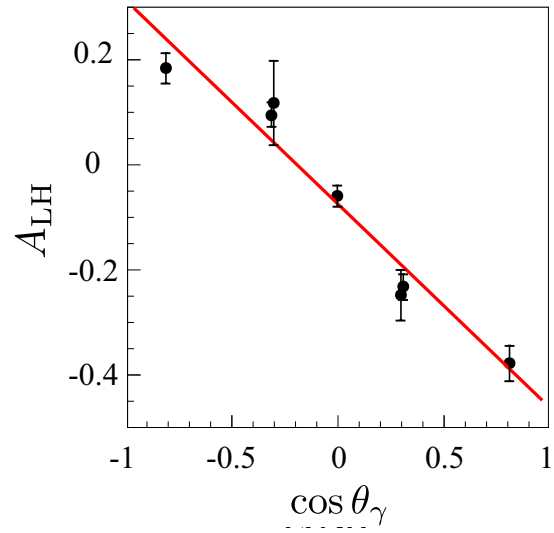

FIG. 16. Angular dependence of A_{LH}. The solid line shows the best fit.

emitted in (n,γ) reactions induced by low-energy neutrons according to s- and p-wave amplitudes [15]. The formalism of the differential cross section of the (n,γ) reaction induced by unpolarized neutrons is described in Appendix E. We use $\boldsymbol{I}$ as the spin of the target nuclei, $\boldsymbol{J}$ as the spin of the compound nucleus, $\boldsymbol{F}$ as the spin of the final state of the γ-ray transition, and $\boldsymbol{l}$ as the orbital angular momentum of the incident neutron. The total neutron spin is defined as $\boldsymbol{j} = \boldsymbol{l} + \boldsymbol{s}$, where $\boldsymbol{s}$ is the neutron spin. The value of j is $1/2$ for s-wave neutrons ($l = 0$) and $j = 1/2, 3/2$ for p-wave neutrons ($l = 1$).

The p-wave resonance and two neighboring s-wave resonances are considered in the negative- and positive-energy region, listed in Table II, in the following analysis. The resonance energy and resonance width measured in this work is adopted to the p-wave resonance ($r = 2$) and the values in Ref. [20] for the negative resonance and positive s-wave resonance ($r = 1$, $r = 3$). The compound-nuclear spin of the negative s-wave resonance is $J_1 = 4$ [20]. The compound-nuclear spin of the p-wave resonance is assumed to be the same as that of the negative s-wave resonance, because both the negative s-wave and the p-wave components were observed in the 5161 keV γ-ray transition, which implies that $J_2 = 4$. Nevertheless, the compound-nuclear spin of the positive s-wave resonance is taken as $J_3 = 3$, because the 5161 keV transition was not adequately observed in the resonance, as shown in Fig. 17. The contributions of far s-wave resonances are assumed to be negligibly small; that is, $\alpha_1 = 0$ in Eq. (E2).

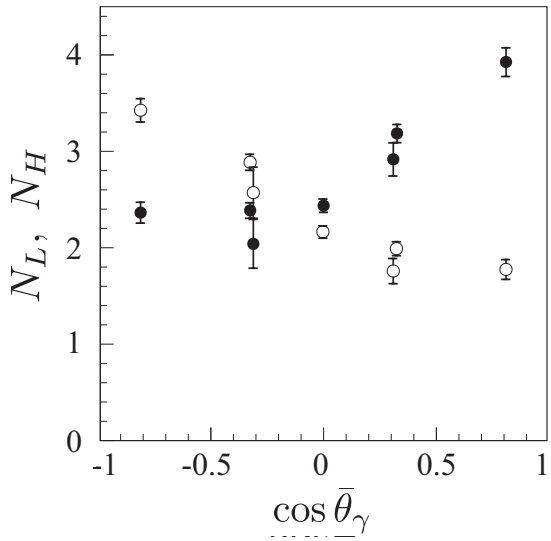

FIG. 15. Angular dependencies of N_L and N_H. The white point and black point show N_L and N_H, respectively.

The ratios of the γ width from each resonance to the ground state can be determined by a comparison of the peak-height ratio of the neutron resonance gated in the 5161 keV photopeak between s_1 wave, p wave, and s_2 wave as

$$\frac{\Gamma^\gamma_{s_1,\mathrm{gnd}}}{\Gamma^\gamma_{s_1}} : \frac{\Gamma^\gamma_{\mathrm{p,gnd}}}{\Gamma^\gamma_{\mathrm{p}}} : \frac{\Gamma^\gamma_{s_2,\mathrm{gnd}}}{\Gamma^\gamma_{s_2,\mathrm{gnd}}} = 1 : 0.796 \pm 0.020 : 0.009 \pm 0.006. \quad (12)$$

As shown in Fig. 17 and in Eq. (12), the branching ratio from the s_2-wave resonance to the ground state is very small. We

TABLE II. Resonance parameters of ^{139}La used in the analysis.

r	E_r [eV]	J_r	l_r	Γ^γ_r [meV]	$g_r\Gamma^n_r$ [meV]	
1	-48.63[a]	4[a]	0	62.2[a]	(571.8)[a,b]	s_1
2	0.740 ± 0.002	4	1	40.41 ± 0.76	$(5.6 \pm 0.5) \times 10^{-5}$ [c]	p
3	72.30 ± 0.05[b]	3	0	75.64 ± 2.21[c]	11.76 ± 0.53[c]	s_2

[a]Taken from Refs. [20,21].
[b]The neutron width for the negative resonance was calculated by using $|E_1|$ instead of E_1.
[c]Taken from Ref. [22].

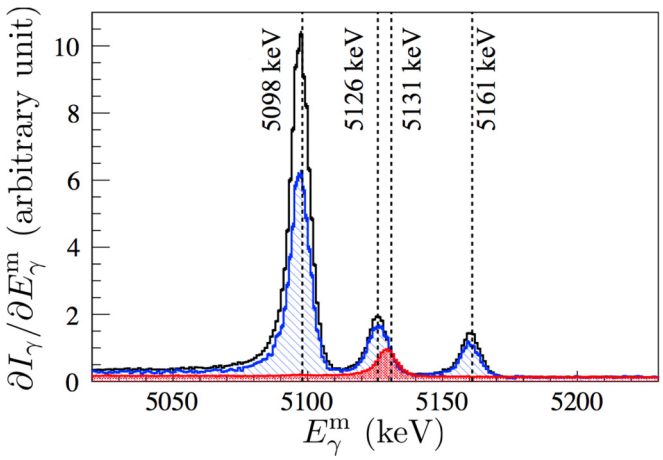

FIG. 17. Comparison of expanded $\partial I_\gamma/\partial E_\gamma^{\rm m}$ gated in the vicinities of s_1-wave resonance ($E_n^{\rm m} = 0.2-0.4$ eV, black line), the p-wave resonance ($E_n^{\rm m} = 0.6-0.9$ eV, shaded area with diagonal line), and the s_2-wave resonance ($E_n^{\rm m} = 70-75$ eV, solid shaded area).

define $(\overline{a_0})_{\rm L}$, $(\overline{a_1})_{\rm L}$, $(\overline{a_3})_{\rm L}$, $(\overline{a_0})_{\rm H}$, $(\overline{a_1})_{\rm H}$, and $(\overline{a_3})_{\rm H}$ as

$$(\overline{a}_{0,1,3})_{\rm L} = \int_{E_p-2\Gamma_p}^{E_p} dE' \int d^3p_A\, a_{0,1,3}\Phi(t^{\rm m}, E', \boldsymbol{p}_A),$$
$$(\overline{a}_{0,1,3})_{\rm H} = \int_{E_p}^{E_p+2\Gamma_p} dE' \int d^3p_A\, a_{0,1,3}\Phi(t^{\rm m}, E', \boldsymbol{p}_A). \quad (13)$$

Here, the a_3 term is ignored because it is proportional to λ_{2f}^2 and is suppressed relative to the s-wave neutron width according to the centrifugal potential by the factor of $(kR)^2$. Under this approximation, Eq. (E1) is reduced to

$$\frac{d\sigma_{n\gamma_f}}{d\Omega_\gamma} = \frac{1}{2}(a_0 + a_1\cos\theta_\gamma). \quad (14)$$

Substituting Eq. (14) into Eqs. (5) and (6), the angular dependence of the γ-ray counts in the neutron-energy regions $E_p - 2\Gamma_p \leqslant E_n \leqslant E_p$ and $E_p \leqslant E_n \leqslant E_p + 2\Gamma_p$ can be written as

$$\left(\frac{\partial^2 I_\gamma}{\partial t^{\rm m}\partial\Omega_\gamma}(t^{\rm m},\Omega_\gamma)\right)_{\rm L} = \frac{I_0}{2}[(\overline{a_0})_{\rm L} + (\overline{a_1})_{\rm L}P_1(\cos\theta_\gamma)],$$
$$\left(\frac{\partial^2 I_\gamma}{\partial t^{\rm m}\partial\Omega_\gamma}(t^{\rm m},\Omega_\gamma)\right)_{\rm H} = \frac{I_0}{2}[(\overline{a_0})_{\rm H} + (\overline{a_1})_{\rm H}P_1(\cos\theta_\gamma)]. \quad (15)$$

By convoluting with Eq. (7), the γ-ray counts $(I_{\gamma,d})_{\rm L}$ and $(I_{\gamma,d})_{\rm H}$ to be measured by the dth detector can be written as

$$(I_{\gamma,d})_{\rm L,H} = \frac{I_0}{2}[(\overline{a_0})_{\rm L,H}\overline{P_{d,0}} + (\overline{a_1})_{\rm L,H}\overline{P_{d,1}}]. \quad (16)$$

Because the energy dependence of x_2 and y_2 is negligibly small in the vicinity of the p-wave resonance ($r_p = 2$), $(\overline{a_1})_{\rm L}$ and $(\overline{a_1})_{\rm H}$ are linear functions of x_2 and y_2 and are thus a function of ϕ_2. The value of ϕ_2 is determined by comparing $[(I_{\gamma,d})_{\rm L} - (I_{\gamma,d})_{\rm H}]/[(I_{\gamma,d})_{\rm L} + (I_{\gamma,d})_{\rm H}]$ with the measured values A in

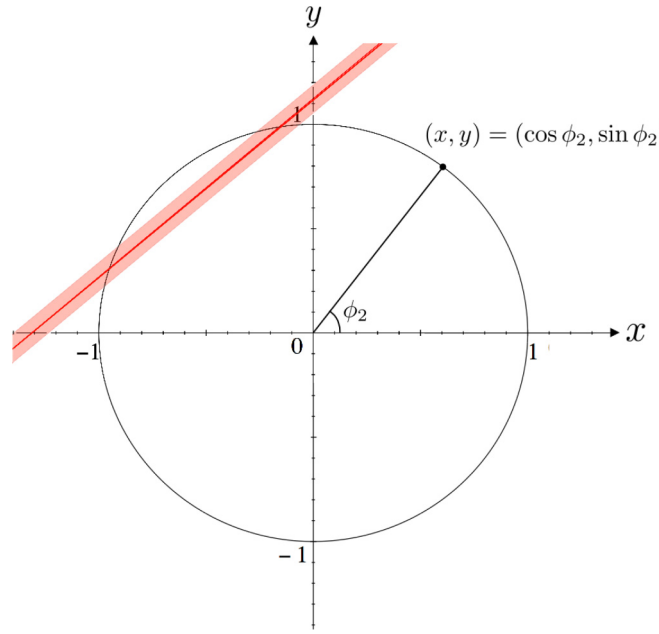

FIG. 18. Visualization of the value of ϕ_2 on the xy plane. The solid line and shaded area show the central values of the ϕ_2 and 1σ area, respectively. ϕ_2 denotes an angle of a point on a unit circle.

Eq. (11):

$$A = \frac{(\overline{a_1})_{\rm L} - (\overline{a_1})_{\rm H}}{(\overline{a_0})_{\rm L} + (\overline{a_0})_{\rm H}} = 0.295\cos\phi_2 - 0.345\sin\phi_2. \quad (17)$$

Two solutions can be obtained as

$$\phi_2 = \left(99.2^{+6.3}_{-5.3}\right)^\circ, \quad \left(161.9^{+5.3}_{-6.3}\right)^\circ. \quad (18)$$

The visualization of ϕ_2 is shown in Fig. 18.

IV. DISCUSSION

Because the value of ϕ_2 was obtained in the previous section, the T-violation sensitivity is discussed in this section. We obtain x_2 from Eqs. (18) and (E5) with resonance number $r_p = 2$ as

$$x_2 = -0.16^{+0.09}_{-0.11}, \quad -0.95^{+0.04}_{-0.03}. \quad (19)$$

This leads to the value of W which is given by Eq. (1) as

$$W = \left(13.2^{+18.1}_{-5.3}\right)\ \text{meV}, \quad \left(2.21^{+0.10}_{-0.06}\right)\ \text{meV}. \quad (20)$$

The published value of $A_{\rm L} = (9.56 \pm 0.35) \times 10^{-2}$ in Ref. [7] and the resonance parameters in Table I are used in the calculation. Note that the neutron width of the negative s-wave resonance $\Gamma_1^{\rm n}$ at the resonance energy of the p-wave resonance is adopted.

The ratio of P-odd T-odd cross sections to P-odd cross sections is given as

$$\frac{\Delta\sigma_{\rm PT}}{\Delta\sigma_p} = \kappa(J)\frac{W_{\rm T}}{W}, \quad (21)$$

where $\Delta\sigma_{\rm PT}$ is the P-odd T-odd cross section, $\Delta\sigma_p$ is the P-odd cross section, $W_{\rm T}$ is the P-odd T-odd matrix element, and W is

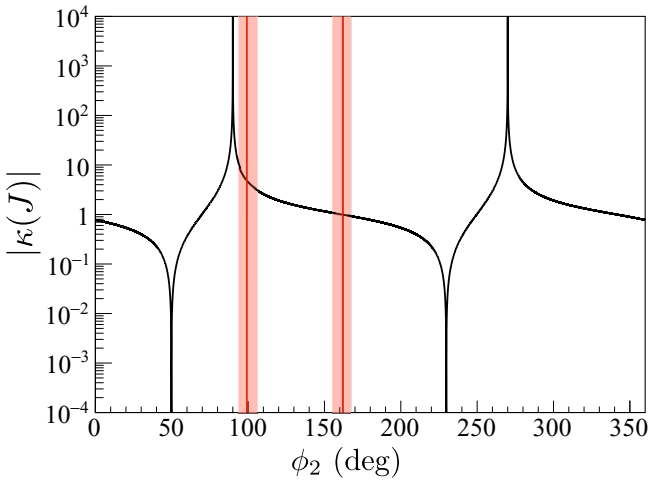

FIG. 19. Value of $|\kappa(J)|$ as a function of ϕ_2. The solid line and shaded area show the central values of ϕ_2 and the 1σ area from the central value, respectively.

the P-odd matrix element [14]. The calculations of these matrix elements were performed in Refs. [25,26]. The spin factor $\kappa(J)$ is defined as

$$\kappa(J) = \begin{cases} (-1)^{2I}\left(1 + \frac{1}{2}\sqrt{\frac{2I-1}{I+1}}\frac{y}{x}\right) & \left(J = I - \frac{1}{2}\right) \\ (-1)^{2I+1}\frac{I}{I+1}\left(1 - \frac{1}{2}\sqrt{\frac{2I+3}{I}}\frac{y}{x}\right) & \left(J = I + \frac{1}{2}\right)\ldots. \end{cases} \tag{22}$$

The magnitude of $\kappa(J)$ indicates the sensitivity to the P-odd T-odd interaction. The $J = I + \frac{1}{2}$ case corresponds to the p-wave resonance of $^{139}\mathrm{La} + n$ at $E_n = E_2$. The value of $\kappa(J)$ corresponding to the ϕ_2 obtained is

$$\kappa(J) = 4.84^{+5.58}_{-1.69}, \quad 0.99^{+0.08}_{-0.07}, \tag{23}$$

and $|\kappa(J)|$ is shown in Fig. 19.

In the previous section, the a_3 term was ignored, because the centrifugal potential of the p-wave resonance is small. Hereafter, we discuss the case when the a_3 term in Eq. (E1) is activated. We analyze the angular dependencies of $N_\mathrm{L} - N_\mathrm{H}$ and $N_\mathrm{L} + N_\mathrm{H}$ fit by the functions of $f(\bar{P}_{d,1}/\bar{P}_{d,0}) = A'\bar{P}_{d,1}/\bar{P}_{d,0} + B'$ and $g(\bar{P}_{d,2}/\bar{P}_{d,0}) = C'\bar{P}_{d,2}/\bar{P}_{d,0} + D'$, respectively, with fitting parameters A', B', C', and D' (see Fig. 20). The equations of a_3 can be written as

$$\frac{A'}{D'} = \frac{(\overline{a_1})_\mathrm{L} - (\overline{a_1})_\mathrm{H}}{(\overline{a_0})_\mathrm{L} + (\overline{a_0})_\mathrm{H}} = 0.295\cos\phi_2 - 0.345\sin\phi_2, \tag{24}$$

$$\frac{C'}{D'} = \frac{(\overline{a_3})_\mathrm{L} + (\overline{a_3})_\mathrm{H}}{(\overline{a_0})_\mathrm{L} + (\overline{a_0})_\mathrm{H}} = -0.295\cos\phi_2\sin\phi_2 + 0.050\sin^2\phi_2. \tag{25}$$

The fit results of C'/D' and A'/D' are

$$\frac{C'}{D'} = 0.191 \pm 0.028, \quad \frac{A'}{D'} = -0.409 \pm 0.024. \tag{26}$$

The value of ϕ_2 is determined by combining Eq. (24) for a_1 and Eq. (25) for a_3 on the xy plane. The result is shown in Fig. 21. The restriction from the a_3 term is not consistent with that of the a_1 term. The a_3 term deviates from the requirement of $x_2^2 + y_2^2 = 1$ by more than 2σ.

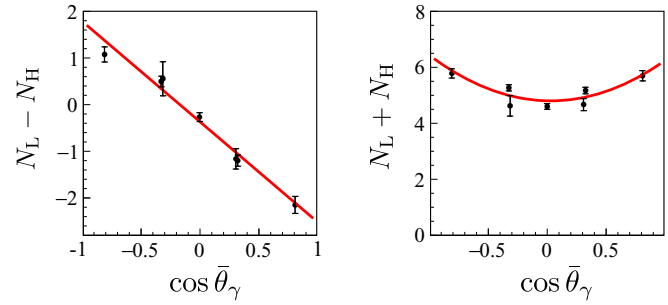

FIG. 20. Angular dependencies of $N_\mathrm{L} - N_\mathrm{H}$ and $N_\mathrm{L} + N_\mathrm{H}$. The solid line indicates the best fit.

In this analysis, $J_1 = J_2 = 4$, $J_3 = 3$ are assumed. However, there is a possibility of the case of $J_1 = J_2 = J_3 = 3$. Because the effect of the s_2 wave is negligibly small in this discussion, we discuss combinations of J_1 and J_2 only. The result of the case of $J_1 = J_2 = J_3 = 3$ is shown in Fig. 22. Both a_1 and a_3 in the case of $J_1 = J_2 = J_3 = 3$ have no solution. As both a_1 and a_3 in the case of $J_1 = J_2 = 4$, $J_3 = 3$ have a solution in 3σ; we support $J_1 = J_2 = 4$.

The origin of the inconsistency has not been identified in the present study. The inconsistency may be due to possible incompleteness of the reaction mechanism based on the interference between s- and p-wave amplitudes with the Breit–Wigner approximation.

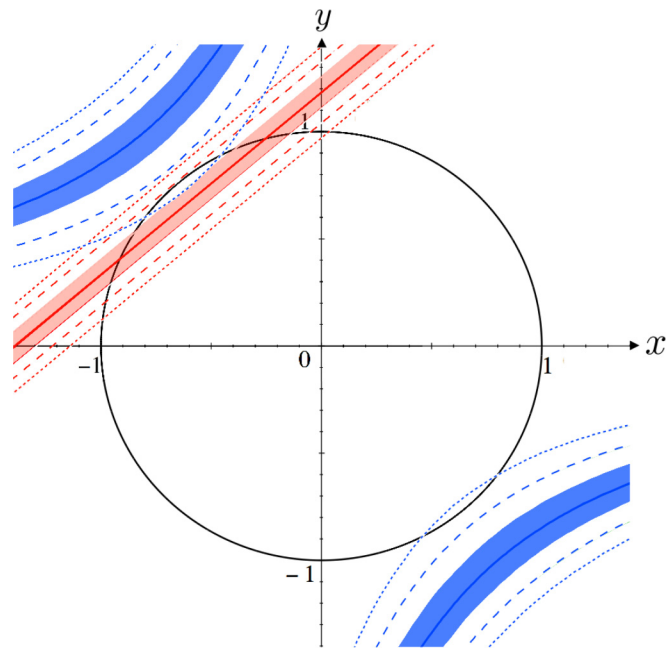

FIG. 21. a_1 (straight lines) and a_3 (curved lines) on the xy plane for the cases of $J_1 = J_2 = 4$, $J_3 = 3$. The solid line, shaded area, dashed line, and dotted line show the central values of ϕ_2, 1σ areas, 2σ contours, and 3σ contours, respectively.

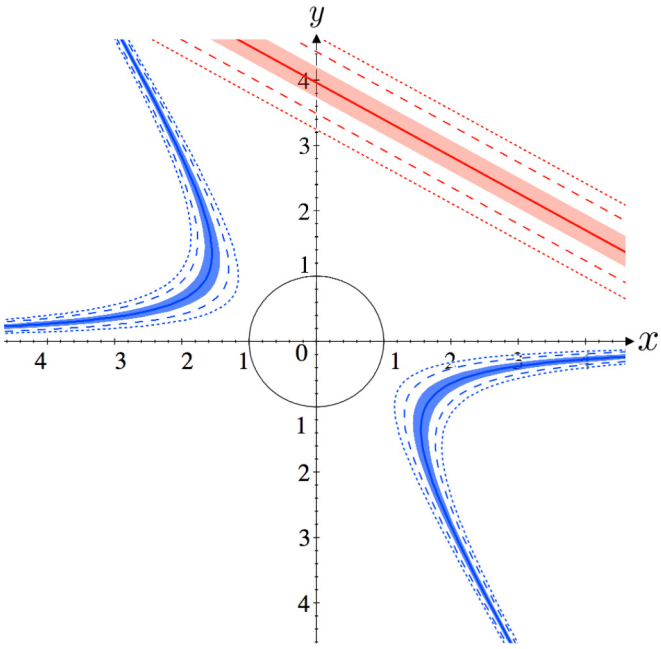

FIG. 22. a_1 (straight lines) and a_3 (curved lines) on the xy plane in the case of $J_1 = J_2 = J_3 = 3$. The solid line, shaded area, dashed line, and dotted line show the central values of ϕ_2, 1σ areas, 2σ contours, and 3σ contours, respectively.

V. CONCLUSION

We observed clear angular distribution of emitted γ rays in the transition from the p-wave resonance of $^{139}\mathrm{La} + n$ to the ground state of $^{140}\mathrm{La}$ as a function of incident neutron energy. The angular distribution was analyzed by assuming interference between s- and p-wave amplitudes, and the partial neutron width of the p-wave resonance was obtained. This result suggests that the T-violating effect can be enhanced at the same order of the P-violating effect for the 0.74 eV p-wave resonance of $^{139}\mathrm{La} + n$. Therefore an experiment to explore T violation in compound-nuclear states is feasible. In addition, the analysis under this assumption leads to results that are consistent with theoretical expectation, and we therefore believe the assumption of s-p mixing is correct.

ACKNOWLEDGMENTS

The authors would like to thank the staff of ANNRI for the maintenance of the germanium detectors, and MLF and J-PARC for operating the accelerators and the neutron-production target. We would like to thank Dr. K. Kino for the calculation of the pulse shape of the neutron beam. We also appreciate the continuous help of Professor V. P. Gudkov for the interpretation of the measured results. The neutron experiments at the Materials and Life Science Experimental Facility of J-PARC were performed under the user program (Proposals No. 2011B0042, No. 2012A0122, No. 2012B0236, No. 2013B0189, No. 2014A0285, No. 2014B0348, No. 2015A0245, No. 2016B0200, No. 2016B0202, No. 2017A0158, No. 2017A0170, and No. 2017A0203). This work was supported by the Neutron Science Division of KEK as S-type research projects with program numbers 2014S03 and 2015S12. This work was partially supported by MEXT KAKENHI Grant No. JP19GS0210 and JSPS KAKENHI Grant No. JP17H02889.

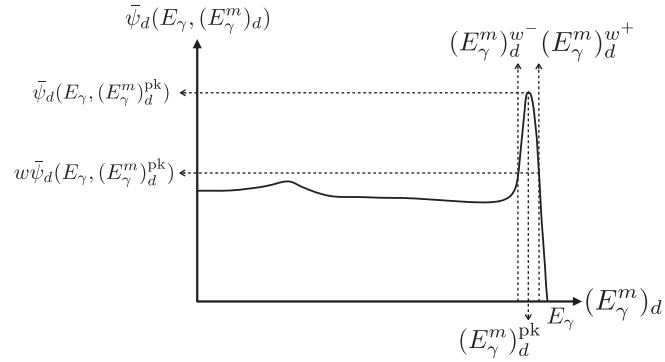

FIG. 23. Schematic of definition of the photopeak in the pulse-height spectrum.

APPENDIX A: DEFINITIONS OF SYMBOLS DESCRIBING DETECTOR CHARACTERISTICS AND RESULTS OF SIMULATION

In this section, we describe the definition of characteristics of the germanium detectors and the simulation results. Herein, we use $\psi_d(E_\gamma,\Omega_\gamma,(E_\gamma^{\mathrm{m}})_d)$ to denote the probability of the case where the energy of $(E_\gamma^{\mathrm{m}})_d$ is deposited in the dth detector, when a γ ray with an energy of E_γ is emitted in the direction of $\Omega_\gamma = (\theta_\gamma,\varphi_\gamma)$. The polar angle and the azimuthal angle of the direction of the emitted γ ray are denoted by θ_γ and φ_γ, respectively. The $\psi_d(E_\gamma,\Omega_\gamma,(E_\gamma^{\mathrm{m}})_d)$ satisfies

$$\int_0^{E_\gamma} \psi_d\left(E_\gamma,\Omega_\gamma,\left(E_\gamma^{\mathrm{m}}\right)_d\right)d\left(E_\gamma^{\mathrm{m}}\right)_d = 1. \tag{A1}$$

We define the distribution of the energy deposit as

$$\bar{\psi}_d\left(E_\gamma,\left(E_\gamma^{\mathrm{m}}\right)_d\right) = \int_{\Omega_d} \psi_d\left(E_\gamma,\Omega_\gamma,\left(E_\gamma^{\mathrm{m}}\right)_d\right)d\Omega_\gamma, \tag{A2}$$

where Ω_d is the geometric solid angle of the dth detector. The photopeak efficiency of the dth detector for γ rays with the energy of E_γ is defined as

$$\epsilon_d^{\mathrm{pk},w}\left(E_\gamma\right) = \int_{(E_\gamma^{\mathrm{m}})_d^{w^-}}^{(E_\gamma^{\mathrm{m}})_d^{w^+}} \bar{\psi}_d\left(E_\gamma,\left(E_\gamma^{\mathrm{m}}\right)_d\right)d\left(E_\gamma^{\mathrm{m}}\right)_d, \tag{A3}$$

where $(E_\gamma^{\mathrm{m}})_d^{w^+}$ and $(E_\gamma^{\mathrm{m}})_d^{w^-}$ are the upper and lower limits of the region of the energy deposit for defining the photopeak region, as schematically shown in Fig. 23. For the definition of the photopeak efficiency $w = 1/4$ was used. The relative photopeak efficiency is also defined as

$$\bar{\epsilon}_d^{\,\mathrm{pk},w}(E_\gamma) = \frac{\epsilon_d^{\mathrm{pk},w}(E_\gamma)}{\epsilon_1^{\mathrm{pk},w}(E_\gamma)}. \tag{A4}$$

The value of $\bar{\psi}_d(E_\gamma,(E_\gamma^{\mathrm{m}})_d)$ was obtained by using the simulation to reproduce the pulse-height spectra for γ rays

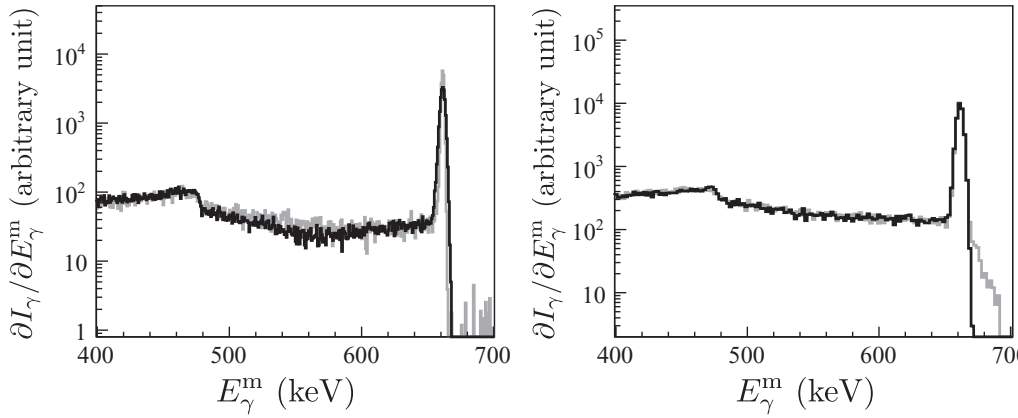

FIG. 24. Comparison of the pulse-height spectrum for γ rays from a radioactive source ^{137}Cs (gray line) and the numerical simulation (black line) for a type-B detector (left) and a type-A detector (right). Because the simulation faithfully reproduces the experimental data, these almost overlap.

from the radioactive source of ^{137}Cs ($E_\gamma = 0.662$ MeV), as shown in Fig. 24. Subsequently, the reproducibility was checked by comparing the pulse-height spectra for ^{60}Co at $E_\gamma = 1.173$ MeV, 1.332 MeV and ^{22}Na at $E_\gamma = 1.275$ MeV. Finally, we confirmed that the simulation program is applicable to higher energies by comparing the numerical simulation with the pulse-height spectrum for prompt γ rays emitted by the ^{14}N(n,γ) reaction at $E_\gamma = 10.829$ MeV, as shown in Fig. 25. The photopeak efficiency of the detector assembly for 1.332 MeV γ ray is determined to be $3.64\% \pm 0.11\%$ [27]. In the case of an angular distribution of γ rays this is expanded by using Legendre polynomials as $\sum_{p=0}^{\infty} c_p P_p(\cos\theta_\gamma)$, and the photopeak counts of the dth detector can be written as

$$N_d(E_\gamma) = N_0 \sum_{p=0}^{\infty} c_p \bar{P}_{d,p},$$

$$\bar{P}_{d,p} = \frac{1}{4\pi} \int_{(E_\gamma^{\rm m})_d^{w-}}^{(E_\gamma^{\rm m})_d^{w+}} d\left(E_\gamma^{\rm m}\right)_d \int d\Omega_\gamma P_p(\cos\theta_\gamma) \bar{\psi}_d(E_\gamma, \Omega_\gamma). \tag{A5}$$

The determined values of $\bar{P}_{d,p}$ are listed in Table III for $p = 0,1,2$. The quantity $\bar{P}_0$ corresponds to $\epsilon_d^{{\rm pk},w}$. The table also contains the weighted average of the viewing angle of each detector $\bar{\theta}_d$ determined as $P_p(\cos\bar{\theta}_d) = \bar{P}_{d,p}/\bar{P}_{d,0}$.

APPENDIX B: NEUTRON ABSORPTION CROSS SECTION

The formula used to describe the neutron cross section $\sigma_{\rm t}$ is given as a function of the neutron energy in the center-of-mass system:

$$\sigma_{\rm t}(E) = \sigma_s + \sigma_{{\rm n}\gamma}(E_n), \tag{B1}$$

$$\sigma_s = 4\pi a^2, \tag{B2}$$

$$\Gamma_r^\gamma = \sum_f \Gamma_{r,f}^\gamma, \tag{B3}$$

$$\sigma_{{\rm n}\gamma}(E_n) = \sum_f \sigma_{n\gamma_f}(E_n), \tag{B4}$$

$$\sigma_{n\gamma_f}(E_n) = \sum_r \frac{\pi\hbar^2}{2m_n E_n} \left[\frac{E_n}{E_r}\right]^{l_r+1/2} \frac{g_r \Gamma_r^n \Gamma_{r,f}^\gamma}{(E_n - E_r)^2 + (\Gamma_r/2)^2}, \tag{B5}$$

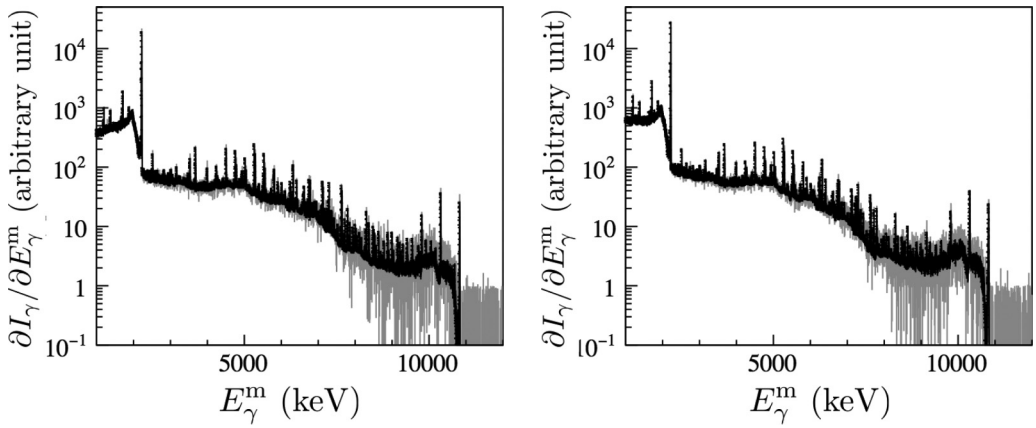

FIG. 25. Comparison of pulse-height spectrum for prompt γ rays emitted in ^{14}N(n,γ) reaction (gray line) and the numerical simulation (black line) for a type-A detector (left) and a type-B detector (right). Because the simulation faithfully reproduces the experimental data, these almost overlap.

TABLE III. Values of $\bar{P}_{d,p}/\bar{P}_{d,0}$ for $p = 1,2$ are shown for all detectors together with the weighted average angle of each detector $\bar{\theta}_d$ at $E_\gamma = 0.662$ MeV and $E_\gamma = 5.262$ MeV. The relative peak efficiency $\bar{\epsilon}_d^{\mathrm{pk},1/4}$ was measured using $^{14}\mathrm{N}(n,\gamma)$ reactions are also shown.

	$E_\gamma = 0.662\,\mathrm{MeV}$			$E_\gamma = 5.262\,\mathrm{MeV}$			
d	$\bar{P}_{d,1}/\bar{P}_{d,0}$	$\bar{P}_{d,2}/\bar{P}_{d,0}$	$\bar{\theta}_d$	$\bar{\epsilon}_d^{\mathrm{pk},1/4}$	$\bar{P}_{d,1}/\bar{P}_{d,0}$	$\bar{P}_{d,2}/\bar{P}_{d,0}$	$\bar{\theta}_d$
1	0.00001 ± 0.00002	−0.488480 ± 0.000003	90.000 ± 0.001	1	−0.00004 ± 0.00004	−0.49036 ± 0.00001	90.002 ± 0.002
2	−0.00003 ± 0.00003	−0.489485 ± 0.000003	90.002 ± 0.001	0.997 ± 0.027	0.00006 ± 0.00004	−0.49115 ± 0.00001	89.997 ± 0.002
3	0.30297 ± 0.00002	−0.35283 ± 0.00002	72.299 ± 0.001	0.920 ± 0.026	0.29887 ± 0.00004	−0.35791 ± 0.00003	72.556 ± 0.002
4	0.30294 ± 0.00002	−0.35285 ± 0.00002	72.301 ± 0.001	1.041 ± 0.028	0.29889 ± 0.00004	−0.35791 ± 0.00003	72.555 ± 0.002
5	0.00008 ± 0.00002	−0.489493 ± 0.000003	89.996 ± 0.001	1.025 ± 0.028	−0.00012 ± 0.00004	−0.49116 ± 0.00001	90.007 ± 0.002
6	−0.30293 ± 0.00002	−0.35288 ± 0.00002	107.698 ± 0.001	1.092 ± 0.029	−0.29886 ± 0.00004	−0.35792 ± 0.00003	107.443 ± 0.002
7	−0.30297 ± 0.00002	−0.35284 ± 0.00002	107.700 ± 0.001	0.999 ± 0.027	−0.29885 ± 0.00004	−0.35794 ± 0.00003	107.442 ± 0.002
8	0.00004 ± 0.00002	−0.488259 ± 0.000003	89.998 ± 0.001	0.923 ± 0.026	0.00005 ± 0.00004	−0.49030 ± 0.00001	89.997 ± 0.002
9	−0.00002 ± 0.00003	−0.48927 ± 0.000003	90.001 ± 0.001	0.915 ± 0.026	−0.00003 ± 0.00004	−0.49107 ± 0.00001	90.002 ± 0.002
10	0.30292 ± 0.00002	−0.35288 ± 0.00002	72.302 ± 0.001	0.998 ± 0.027	0.29894 ± 0.00004	−0.35785 ± 0.00003	72.552 ± 0.002
11	0.30297 ± 0.00002	−0.35284 ± 0.00002	72.300 ± 0.001	0.945 ± 0.026	0.29886 ± 0.00004	−0.35793 ± 0.00003	72.557 ± 0.002
12	−0.00001 ± 0.00003	−0.489256 ± 0.000003	90.001 ± 0.001	0.979 ± 0.027	0.00004 ± 0.00004	−0.49108 ± 0.00001	89.997 ± 0.002
13	−0.30293 ± 0.00002	−0.35286 ± 0.00002	107.698 ± 0.001	1.046 ± 0.028	−0.29892 ± 0.00004	−0.357867 ± 0.00003	107.447 ± 0.002
14	−0.30297 ± 0.00002	−0.35284 ± 0.00002	107.700 ± 0.001	1.142 ± 0.030	−0.29887 ± 0.00004	−0.35791 ± 0.00003	107.444 ± 0.002
15	−0.80431 ± 0.00001	0.47410 ± 0.00004	143.824 ± 0.001	0.892 ± 0.025	−0.80420 ± 0.00002	0.47340 ± 0.00005	143.780 ± 0.002
16	−0.30772 ± 0.00003	−0.35142 ± 0.00003	107.967 ± 0.002	0.356 ± 0.014	−0.30775 ± 0.00004	−0.35229 ± 0.00004	107.963 ± 0.003
17	0.30697 ± 0.00002	−0.34904 ± 0.00002	72.058 ± 0.001	0.945 ± 0.026	0.30715 ± 0.00004	−0.34994 ± 0.00003	72.054 ± 0.002
18	0.80434 ± 0.00001	0.47419 ± 0.00004	36.173 ± 0.001	1.170 ± 0.031	0.80418 ± 0.00002	0.47337 ± 0.00005	36.221 ± 0.002
19	0.80425 ± 0.00001	0.47396 ± 0.00004	36.182 ± 0.001	0.917 ± 0.026	0.80415 ± 0.00002	0.47328 ± 0.00005	36.225 ± 0.002
20	0.30683 ± 0.00002	−0.34917 ± 0.00002	72.066 ± 0.001		0.30705 ± 0.00004	−0.35004 ± 0.00003	72.060 ± 0.002
21	−0.30689 ± 0.00002	−0.34911 ± 0.00002	107.938 ± 0.001		−0.30709 ± 0.00004	−0.34999 ± 0.00003	107.943 ± 0.002
22	−0.80427 ± 0.00001	0.47401 ± 0.00004	143.820 ± 0.001	1.113 ± 0.030	−0.80420 ± 0.00002	0.47341 ± 0.00005	143.781 ± 0.002

where σ_s is the scattering cross section, $\sigma_{\mathrm{n}\gamma}$ is the radiative capture cross section, $k_n = \sqrt{2m_n E_n}/\hbar$, a are scattering length, E_r is the resonance energy of the rth resonance, $g_r = (2J_r + 1)/[2(2I + 1)]$ is the statistical factor with the target nuclear spin I and the spin of the rth resonance J_r, Γ_r^n is the neutron width of rth resonance, and $\Gamma_{r,f}^\gamma$ is the γ width of the γ-ray transition from the rth resonance to the final state f. The quantity l_r represents the orbital angular momentum of the incident neutrons contributing to rth resonance. The above formula is valid for $l_r = 0,1$. Higher angular momenta can be ignored in the incident-neutron-energy region of interest.

APPENDIX C: PULSE SHAPE OF NEUTRON BEAM

The pulse shape of the neutron beam depends on the neutron energy E_n according to the time delay during the moderation process. The double differential of the flux of the pulsed neutron beam I_n as a function of E_n, and the time measured from the primary proton beam injection t, is known to be well reproduced by the Ikeda–Carpenter function, defined as

$$\frac{\partial^2 I_n}{\partial E_n \partial t}(E_n,t) = \frac{\alpha C}{2}\left\{(1-R)(\alpha t)^2 e^{-\alpha t} + 2R\frac{\alpha^2\beta}{(\alpha-\beta)^3} \times\left[e^{-\beta t} - e^{-\alpha t}\left(1 + (\alpha-\beta)t + \frac{(\alpha-\beta)^2}{2}t^2\right)\right]\right\}, \quad \text{(C1)}$$

where parameters α, β, C, R depend on E_n. The Ikeda–Carpenter function was originally proposed to explain the pulse shape of the cold source of polyethylene moderators at the Intense Pulsed Neutron Source of the Argonne National Laboratory [28]. The double differential of the neutron beam flux on the moderator surface of the J-PARC spallation source was calculated by using MCNPX [29], and was fit with the Ikeda–Carpenter function. The dependence of neutron energy on the fitting parameters t_0, α, β, R, and C were obtained by fitting of the pulse shape of neutron beam with a polynomial function [17].

The energy spectrum at a given time t^{m} at a distance L from the moderator surface is given as

$$\frac{\partial I_n}{\partial t^{\mathrm{m}}}(t^{\mathrm{m}}) = \int dE' \frac{\partial^2 I_{\mathrm{n}}}{\partial E_n \partial t}\left(E', t^{\mathrm{m}} - L\sqrt{\frac{m_n}{2E'}}\right). \quad \text{(C2)}$$

APPENDIX D: THERMAL MOTION OF TARGET NUCLEUS

We adopted the free gas model for the thermal motion of the target nuclei, which leads to a γ-ray yield in the form of

$$\frac{\partial I_\gamma}{\partial t^{\mathrm{m}}}(t^{\mathrm{m}}) = I_0 \int dE' d^3 p_A \frac{\partial^2 I_n}{\partial E_n \partial t}\left(E', t^{\mathrm{m}} - L\sqrt{\frac{m_n}{2E'}}\right) \times \frac{1}{(2\pi m_A k_{\mathrm{B}} T)^{3/2}} e^{-p_A^2/2m_A k_{\mathrm{B}} T} \times \frac{\sigma_{n\gamma}(E_n)}{\sigma_{\mathrm{t}}(E_n)}(1 - e^{-n\sigma_{\mathrm{t}}(E)\,\Delta z}), \quad \text{(D1)}$$

as long as the target is sufficiently thin such that multiple scattering is negligible. I_0 is the normalization constant, Δz is the target thickness, n is the number density of target nuclei, k_B is the Boltzmann constant, and T is the effective temperature of the target, which can be used as a fitting parameter.

APPENDIX E: FORMULA DESCRIBING (n,γ) ANGULAR DEPENDENCE

The differential cross section of the (n,γ) reaction induced by unpolarized neutrons can be written as

$$\begin{aligned}
\frac{d\sigma_{n\gamma_f}}{d\Omega_\gamma} &= \frac{1}{2}\left[a_0 + a_1\cos\theta_\gamma + a_3\left(\cos^2\theta_\gamma - \frac{1}{3}\right)\right],\\
a_0 &= \sum_{r_s}\left|V_{r_s}\right|^2 + \sum_{r_p}\left|V_{r_p}\right|^2,\\
a_1 &= 2\mathrm{Re}\sum_{r_s i_p j} V_{r_s}V^*_{r_p} z_{r_p j} P\left(J_{r_s} J_{r_p} \frac{1}{2} j 1 I F\right),\\
a_3 &= 3\sqrt{10}\,\mathrm{Re}\sum_{r_p j r'_p j'} V_{r_p}V^*_{r'_p} z_{r_p j} z_{r_p j'} P\left(J_{r_p} J_{r'_p} j j' 2 I F\right)\begin{Bmatrix} 2 & 1 & 1\\ 0 & 1/2 & 1/2\\ 2 & r_p & j'\end{Bmatrix},
\end{aligned} \tag{E1}$$

$$\begin{aligned}
V_{r_s f} &= -\frac{\sqrt{g_{r_s}}}{2k_n}\frac{\sqrt{\Gamma^n_{r_s}\Gamma^\gamma_{r_s f}}\left(1+\alpha_{r_s}\right)}{E_n - E_{r_s} + i\Gamma_{r_s}/2},\\
V_{r_p f} &= -\frac{\sqrt{g_{r_p}}}{2k_n}\frac{\sqrt{\Gamma^n_{r_p}\Gamma^\gamma_{r_p f}}}{E_n - E_{r_p} + i\Gamma_{r_p}/2},\\
z_{r_p j} &= \sqrt{\frac{\Gamma^n_{r_p j}}{\Gamma^n_{r_p}}} = \begin{cases} x_{r_p} & (j = 1/2)\\ y_{r_p} & (j = 3/2),\end{cases}
\end{aligned}$$

$$P(JJ'jj'kIF) = (-1)^{J+J'+j'+I+F}\frac{3}{2}\sqrt{(2J+1)(2J'+1)(2j+1)(2j'+1)}\begin{Bmatrix} k & j & j'\\ I & J' & J\end{Bmatrix}\begin{Bmatrix} k & 1 & 1\\ F & J & J'\end{Bmatrix}, \tag{E2}$$

where r_s is the rth s-wave resonance number ($l_{r_s} = 0$) and r_p is the r^{th} p-wave resonance number ($l_{r_p} = 1$). Amplitudes V_{r_s} and V_{r_p} are the s- and p-wave amplitudes, respectively, and α_{r_s} represents the contribution from far s-wave resonances. The width $\Gamma^n_{r_p j}$ is the partial neutron width for the incident neutrons of total angular momentum of j, and x_{r_p} and y_{r_p} are defined as

$$x_{r_p} = \sqrt{\frac{\Gamma^n_{p,j=1/2}}{\Gamma^n_p}}, \quad y_{r_s} = \sqrt{\frac{\Gamma^n_{p,j=3/2}}{\Gamma^n_p}}. \tag{E3}$$

x_{r_p} and y_{r_p} satisfy

$$x^2_{r_p} + y^2_{r_p} = 1 \tag{E4}$$

due to the relation $\Gamma^n_p = \Gamma^n_{p,j=1/2} + \Gamma^n_{p,j=3/2}$. The resonance energy and the resonance width obtained from this experiment, the published values listed in Table I, and $I = 7/2$ are used to determine the value of ϕ_{r_p}, defined as

$$x_{r_p} = \cos\phi_{r_p}, \quad y_{r_p} = \sin\phi_{r_p}. \tag{E5}$$

In the case of ^{139}La, negative s-wave amplitude V_1, p-wave amplitude V_2, and positive s-wave amplitude V_3 can be written as

$$V_{1f} = -\lambda_{1f}\left(\frac{|E_1|}{E_n}\right)^{\frac{1}{4}}\frac{\Gamma_1/2}{E_n - E_1 + i\Gamma_1/2}, \quad V_{2f} = -\lambda_{2f}\left(\frac{E_n}{E_2}\right)^{\frac{1}{4}}\frac{\Gamma_2/2}{E_n - E_2 + i\Gamma_2/2}, \quad V_{3f} = -\lambda_{3f}\left(\frac{E_3}{E_n}\right)^{\frac{1}{4}}\frac{\Gamma_3/2}{E_n - E_3 + i\Gamma_3/2}, \tag{E6}$$

where the absolute value of E_1 is adopted simply to avoid the imaginary neutron width. The terms a_0, a_1, and a_3 are given as

$$a_0 = \lambda_{1f}^2\sqrt{\frac{|E_1|}{E_n}}\frac{\Gamma_1^2/4}{(E_n-E_1)^2+\Gamma_1^2/4} + \lambda_{2f}^2\sqrt{\frac{E_n}{E_2}}\frac{\Gamma_2^2/4}{(E_n-E_2)^2+\Gamma_2^2/4} + \lambda_{3f}^2\sqrt{\frac{E_3}{E_n}}\frac{\Gamma_3^2/4}{(E_n-E_3)^2+\Gamma_3^2/4},$$

$$a_1 = \lambda_{1f}\lambda_{2f}\left(\frac{|E_1|}{E_2}\right)^{\frac{1}{4}}\frac{\Gamma_1\Gamma_2(E_n-E_1)(E_n-E_2)+\Gamma_1^2\Gamma_2^2/4}{2\left[(E_n-E_1)^2+\Gamma_1^2/4\right]\left[(E_n-E_2)^2+\Gamma_2^2/4\right]}\frac{5}{8}\left(-x+\sqrt{\frac{7}{5}}y\right)$$
$$+\lambda_{3f}\lambda_{2f}\left(\frac{E_3}{E_2}\right)^{\frac{1}{4}}\frac{\Gamma_3\Gamma_2(E_n-E_3)(E_n-E_2)+\Gamma_3^2\Gamma_2^2/4}{2\left[(E_n-E_3)^2+\Gamma_3^2/4\right]\left[(E_n-E_2)^2+\Gamma_2^2/4\right]}\frac{3\sqrt{3}}{8}\left(x+\sqrt{\frac{5}{7}}y\right),$$

$$a_3 = \lambda_{2f}^2\sqrt{\frac{E_n}{E_2}}\frac{\Gamma_2^2/4}{(E_n-E_2)^2+\Gamma_2^2/4}\frac{33}{280}(-\sqrt{35}xy+y^2). \tag{E7}$$

It can be assumed that the energy dependence of the neutron width of the rth resonance is given as

$$\Gamma_r^n = (k_n R)^{2l_r}\sqrt{\frac{E_n}{1\,\mathrm{eV}}}\Gamma_r^{nl_r} \tag{E8}$$

for $E_n > 0$ where R is the radius of target nuclei and $\Gamma_r^{nl_r}$ is the reduced neutron width. This energy dependence is implemented as

$$\Gamma_r^n = \left(\frac{E_n}{|E_r|}\right)^{l_r+\frac{1}{2}}\overline{\Gamma_r^n}, \tag{E9}$$

where $\overline{\Gamma_r^n}$ is a constant independent of the energy. As the phase shift due to the optical potential is negligibly small, each amplitude can be written as

$$V_{rf} = -\lambda_{rf}\left(\frac{E_n}{|E_r|}\right)^{\frac{l_r}{2}-\frac{1}{4}}\frac{\Gamma_r/2}{E_n-E_r+i\Gamma_r/2}, \tag{E10}$$

where λ_{rf} is defined as

$$\lambda_{rf} = \frac{\hbar}{2}\sqrt{\frac{2g_r\overline{\Gamma_r^n}\Gamma_{rf}^\gamma}{m_n|E_r|\Gamma_r^2}}. \tag{E11}$$

Γ_{rf}^γ is the γ width from the rth resonance to the final state.

[1] J. M. Potter, J. D. Bowman, C. F. Hwang, J. L. McKibben, R. E. Mischke, D. E. Nagle, P. G. Debrunner, H. Frauenfelder, and L. B. Sorensen, Phys. Rev. Lett. **33**, 1307 (1974).

[2] V. Yuan, H. Frauenfelder, R. W. Harper, J. D. Bowman, R. Carlini, D. W. MacArthur, R. E. Mischke, D. E. Nagle, R. L. Talaga, and A. B. McDonald, Phys. Rev. Lett. **57**, 1680 (1986).

[3] E. G. Adelberger and W. C. Haxton, Annu. Rev. Nucl. Part. Sci. **35**, 501 (1985).

[4] V. P. Alfimenkov, S. B. Borzakov, V. V. Thuan, Y. D. Mareev, L. B. Pikelner, A. S. Khrykin, and E. I. Sharapov, Nucl. Phys. A **398**, 93 (1983).

[5] O. P. Sushkov and V. V. Flambaum, Usp. Fiz. Nauk **136**, 3 (1982).

[6] O. P. Sushkov and V. V. Flambaum, Sov. Phys. Usp. **25**, 1 (1982).

[7] C. D. Bowman, J. D. Bowman, and V. W. Yuan, Phys. Rev. C **39**, 1721 (1989).

[8] V. W. Yuan, C. D. Bowman, J. D. Bowman, J. E. Bush, P. P. J. Delheij, C. M. Frankle, C. R. Gould, D. G. Haase, J. N. Knudson, G. E. Mitchell, S. Penttilä, H. Postma, N. R. Roberson, S. J. Seestrom, J. J. Szymanski, and X. Zhu, Phys. Rev. C **44**, 2187 (1991).

[9] Y. Masuda, T. Adachi, A. Masaike, and K. Morimoto, Nucl. Phys. A **504**, 269 (1989).

[10] H. M. Shimizu, T. Adachi, S. Ishimoto, A. Masaike, Y. Masuda, and K. Morimoto, Nucl. Phys. A **552**, 293 (1993).

[11] H. M. Shimizu, Ph.D. thesis, Kyoto University, 1992.

[12] G. E. Mitchell, J. D. Bowman, S. I. Pentillä, and E. I. Sharapov, Phys. Rep. **354**, 157 (2001).

[13] V. P. Gudkov, Phys. Rep. **212**, 77 (1992).

[14] V. P. Gudkov and H. M. Shimizu, arXiv:1710.02193v1.

[15] V. V. Flambaum and O. P. Sushkov, Nucl. Phys. A **435**, 352 (1985).

[16] M. Igashira, Y. Kiyanagi, and M. Oshima, Nucl. Instrum. Methods Phys. Res., Sect. A **600**, 332 (2009).

[17] K. Kino, M. Furusaka, F. Hiraga, T. Kamiyama, Y. Kiyanagi, K. Furutaka, S. Goko, H. Harada, M. Harada, T. Kai, A. Kimura, T. Kin, F. Kitatani, M. Koizumi, F. Maekawa, S. Meigo, S. Nakamura, M. Ooi, M. Ohta, M. Oshima, Y. Toh, M. Igashira, T. Katabuchi, and M. Mizumoto, Nucl. Instrum. Methods Phys. Res., Sect. A **626-627**, 58 (2011).

[18] A. Kimura *et al.*, J. Nucl. Sci. Technol. (Abingdon, UK) **49**, 708 (2012).
[19] CAEN, http://www.caen.it/, accessed: 2017-10-01.
[20] S. F. Mughabghab, *Atlas of Neutron Resonances*, 5th ed. (Elsevier, Amsterdam, 2006).
[21] K. Shibata, O. Iwamoto, T. Nakagawa, N. Iwamoto, A. Ichihara, S. Kunieda, S. Chiba, K. Furutaka, N. Otuka, T. Ohsawa, T. Murata, H. Matsunobu, A. Zukeran, S. Kamada, and J. Katakura, J. Nucl. Sci. Technol. (Abingdon, UK) **48**, 1 (2011).
[22] R. Terlizzi *et al.* (n_TOF Collaboration), Phys. Rev. C **75**, 035807 (2007).
[23] G. Hacken, J. Rainwater, H. I. Liou, and U. N. Singh, Phys. Rev. C **13**, 1884 (1976).
[24] N. Nica, Nucl. Data Sheets **108**, 1287 (2007).
[25] V. V. Flambaum and O. K. Vorov, Phys. Rev. Lett. **70**, 4051 (1993).
[26] V. V. Flambaum and O. K. Vorov, Phys. Rev. C **51**, 2914 (1995).
[27] T. Kin *et al.*, The 2009 NSS-MIC Conference Record, Orland, USA, October 2009, 1194.
[28] S. Ikeda and J. M. Carpenter, Nucl. Instrum. Methods Phys. Res., Sect. A **239**, 536 (1985).
[29] H. Ikeda, Nucl. Instrum. Methods Phys. Res., Sect. A **600**, 1 (2009).